

DarkAI: I. Mapping the large-scale density field of dark matter using AI

Zitong Wang,¹ Feng Shi,^{1*} Xiaohu Yang,^{2,3} Qingyang Li,^{2,4} Yanming Liu¹ and Xiaoping Li¹

¹*School of Aerospace Science And Technology, Xidian University, Xi'an 710126, People's Republic of China*

²*Department of Astronomy, School of Physics and Astronomy, and Shanghai Key Laboratory for Particle Physics and Cosmology, Shanghai Jiao Tong University, Shanghai 200240, People's Republic of China*

³*Tsung-Dao Lee Institute and Key Laboratory for Particle Physics, Astrophysics and Cosmology, Ministry of Education, Shanghai Jiao Tong University, Shanghai 200240, People's Republic of China*

⁴*Institute for Astronomy, University of Edinburgh, Royal Observatory, Edinburgh EH9 3HJ, United Kingdom*

Accepted XXX. Received YYY; in original form ZZZ

ABSTRACT

We develop a deep learning technique to reconstruct the dark matter density field from the redshift-space distribution of dark matter halos. We implement a UNet-architecture neural network and successfully trained it using the COLA fast simulation, which is an approximation of the N-body simulation with 512^3 particles in a box size of $500 h^{-1}\text{Mpc}$. We evaluate the resulting UNet model not only using the training-like test samples, but also using the typical N-body simulations, including the Jiutian simulation which has 6144^3 particles in a box size of $1000 h^{-1}\text{Mpc}$, and the ELUCID simulation which has a different cosmology. The real-space dark matter density fields in the three simulations can all be recovered consistently with only a small reduction of the cross-correlation power spectrum at 1% and 10% levels at $k = 0.1$ and $0.3 h\text{Mpc}^{-1}$, respectively. It is evident that the reconstruction helps to correct for the redshift-space distortions and is unaffected by the different cosmologies between the training sample (**Planck2018**) and the test sample (**WMAP5**). In addition, we tested the application of the UNet-reconstructed density field to recover the velocity & tidal field and found it outperforms the traditional approach based on the linear bias model, showing a 12.2 percent improvement in the correlation slope and a 21.1 percent reduction in the scatter between the predicted and the true velocities. As a result, our method is highly efficient and has an outstanding level of extrapolation reliability beyond the training set. This offers an optimal solution that determines the three-dimensional underlying density field from the abundant galaxy survey data.

Key words: methods: statistical – galaxies: halos – dark matter – large-scale structure of Universe.

1 INTRODUCTION

Mapping the distributions of galaxies offers a key observational probe to the large-scale mass distribution in the universe, thereby constraining cosmological models (e.g. Fisher et al. 1994; Peacock et al. 2001; Hawkins et al. 2003; Yang et al. 2008; Tinker et al. 2005; Shi et al. 2018), understanding galaxy formation (e.g. Jing et al. 1998; Peacock & Smith 2000; Yang et al. 2003, 2012) and exploring the evolution of the real universe (e.g. Wang et al. 2014, 2016; Tweed et al. 2017). One of the main goals of large redshift surveys of galaxies, such as the 2-degree Field Galaxy Redshift Survey (2dFGRS, Colless et al. 2001) and the Sloan Digital Sky Survey (SDSS, York et al. 2000) is, therefore, to provide a database for studying the three-dimensional distribution of galaxies as accurately as possible. In the next decade, upcoming galaxy surveys such as Dark Energy Spectroscopic Instrument (DESI, DESI Collaboration et al. 2016a,b), Large Synoptic Survey Telescope (LSST, Ivezić et al. 2019), EUCLID (Laureijs et al. 2011), Wide Field Infrared Survey Telescope (WFIRST, Akeson et al. 2019) and Chinese Space Station Telescope (CSST, Zhan 2011; Gong et al. 2019), will map out an unprecedented large volume of the Universe with extraordinary precision. It is then vital to have

an optimal method that can accurately and efficiently determine the three-dimensional underlying density field from the abundant galaxy survey data.

However, a key problem of this endeavor is that galaxies are biased tracers of the mass distribution and one has to understand the relationship between galaxies and dark matter before using the galaxy distribution in space to study the mass distribution in the Universe. In the past two decades, tremendous amounts of effort have been put into the establishment of the relationship between galaxies and dark matter halos, as parameterized either via the conditional luminosity function (CLF) or the halo occupation distribution (HOD) (e.g. Jing et al. 1998; Peacock & Smith 2000; Yang et al. 2003; van den Bosch et al. 2003, 2007; Zheng et al. 2005; Tinker et al. 2005; Mandelbaum et al. 2006; Brown et al. 2008; More et al. 2009; Cacciato et al. 2009; Neistein et al. 2011; Avila-Reese et al. 2011; Leauthaud et al. 2012). An empirical way to establish the galaxy–halo connection is to use galaxy groups, provided that they are defined as sets of galaxies that reside in the same dark matter halo. Yang et al. (2005, 2007, 2021) have developed a halo-based group finder that is optimized for grouping galaxies residing in the same dark matter halos, making it ideally suited for the study of the relation between galaxies and dark matter halos. Thanks to the well-understood galaxy-halo relationship, it affords the opportunity to reconstruct the underlying cosmic density

* E-mail: fshi@xidian.edu.cn

field using the dark halos that are represented by galaxy systems, allowing us to study in detail the relationships among galaxies, dark halos, and large-scale structure (LSS).

Reconstructing the cosmic density field from galaxy distribution has been carried out earlier based on various redshift surveys (e.g. Fisher et al. 1995; Zaroubi et al. 1995; Schmoldt et al. 1999; Mathis et al. 2002; Erdoğdu et al. 2004; Wang et al. 2009, 2013). In these investigations, the distribution of galaxies is usually smoothed heavily and normalized to represent the cosmic density field on large scales. The Wiener reconstruction method, used in Fisher et al. (1995) and Zaroubi et al. (1995), can produce a reconstructed field with the minimum mean square error by assuming that the mass density at a given point is a linear combination of the observed galaxy density field values at various points. The method used in Wang et al. (2009, 2012, 2013) is based on dark matter halos represented by galaxy groups (Yang et al. 2005, 2007, 2012) by considering the halos linearly biased to the underlying density field. Additionally, in the linear theory of gravitational instability, the gravity and velocity vectors are parallel and related to each other by a proportionality constant which depends only on the mean mass density of the Universe, Ω_m . It is possible to determine the gravity field from the galaxy distribution and afterward infer the linear velocity field if one can reconstruct the density field from the galaxy distribution (Wang et al. 2009, 2013).

There are several complications, however, in reconstructing the density and velocity field from galaxy groups or halos. First, as already mentioned, one must adopt some prescriptions for relating the fluctuations in the halos distribution to those in the mass by assuming that the two are related by a linear bias parameter b . However, this model is motivated more by simplicity than by physical principles as the bias parameter b is dependent on scale. The simple proportionality between the gravity and velocity fields in linear theory is valid only when the density fluctuations are small. Once the clustering has become non-linear, this one-to-one correspondence will be erased due to shell crossing. Another problem arises from the redshift-space distortions (RSDs) that the spatial distribution of galaxies observed in redshift space is distorted with respect to the real-space distribution (Sargent & Turner 1977; Davis & Peebles 1983; Kaiser 1987; Hamilton 1992) since redshifts of galaxies are not exact measures of distances because of the peculiar motions of galaxies. On large scales, coherent flows induced by the gravitational action of LSS enhance structure along the line-of-sight (the Kaiser effect, Kaiser 1987). On small scales, the virialized motion of galaxies within dark matter haloes smears out structure along the line-of-sight (the Finger-of-God (FOG) effect, Jackson 1972; Tully & Fisher 1978). The approaches adopted earlier to deal with redshift distortions in reconstruction have been hampered by the fact that the large-scale Kaiser effect and the small-scale FOG effect are interwoven, causing modeling the bias parameters more complicated with its form not to be known a priori (Li et al. 2016; Shi et al. 2016). There are several methods of correcting for distortions to recover the real space density and velocity fields. The studies that use either linear theory or the Zelovich approximation are therefore ultimately very limited in their ability to reconstruct the high-density regions. Thus, in order to make full use of galaxy redshift surveys to map the large-scale structure of the universe, a change of tactics is needed.

In recent years deep learning methods have started to be used in cosmology and LSS, such as estimating cosmological parameters from the dark matter distribution (Ravanbakhsh et al. 2017; Pan et al. 2020), predicting the cosmological structure formation (Lucie-Smith et al. 2018; He et al. 2019), populating the halo position and mass field from the non-linear matter field (Modi et al. 2018; Lucie-Smith et al. 2019; Berger & Stein 2019; Kodi Ramanah et al. 2019), classi-

fying the LSS of the universe (Aragon-Calvo 2019), simulating the underlying luminosity function of a Line intensity maps (Pfeffer et al. 2019), learning the relation between galaxy distribution in hydrodynamic simulations and its underlying dark matter distribution (Zhang et al. 2019; Tröster et al. 2019), reconstructing the baryon acoustic oscillations (BAO) signal (Mao et al. 2021), and reconstructing the non-linear velocity field (Wu et al. 2021, 2023). The ability of these models to learn complex functions has motivated many studies to use them to understand the physics of LSS. However, training the neural network requires a concerted effort of accurate and fast predictions of the universe’s structure. An N-body simulation is an effective approach for predicting the structure formation of the Universe, but it poses a significant computational challenge to evolve the dynamics of the simulation’s billions of particles.

In this paper, we develop a deep-learning technique to predict the real-space density field of dark matter from the redshift-space field of dark matter halos. We process the training based on a fast N-body simulation, which is produced by COMoving Lagrangian Acceleration (COLA) method (Tassev et al. 2013). Unlike standard N-body methods, the COLA method can straightforwardly trade accuracy at small scales for computational speed without sacrificing accuracy at large scales. This is particularly helpful for quickly and affordably generating the large ensembles of accurate mock halo catalogs required to study the reconstruction of the dark matter density field. We will show that the neural network, trained using a limited set of COLA samples, is accurately extrapolated far beyond its training data.

This paper is organized as follows. In Section 2, we present the dataset for generating the training and testing sample used in this paper. In Section 3, we provide a AI-based technique for reconstructing the dark matter density field. We evaluate the accuracy of the reconstructed density field in Section 4 and Section 5. We verify the application of the AI-reconstructed density field to the reconstruction of the velocity & tidal field in Section 6. Finally, we summarize our main finding in Section 7.

2 DATASETS

The training and testing samples are generated using `cola_halo`¹ code (Koda et al. 2016). It generates random Gaussian initial condition with second-order Lagrangian Perturbation Theory (2LPT) (Crocce et al. 2006), evolves the N-body particles with the COMoving Lagrangian Acceleration (COLA) (Tassev et al. 2013) fast simulation method and finds the dark matter haloes with the friends-of-friends algorithm (Davis et al. 1985). By combining 2LPT and N-body code, which is used respectively to solve for large- and small-scale dynamics, a COLA-based simulation run is orders of magnitude faster than a standard detailed N-body simulation.

We generated a set of 30 simulations with independent initial conditions. The cosmological parameters were set with $\Omega_m = 0.3111$, $\Omega_\Lambda = 0.6889$, $h = 0.6766$, and $\sigma_8 = 0.812$. Each of the simulations evolved with 512^3 dark matter particles in a periodic box of $500 h^{-1}$ Mpc. We used the particle and halo distribution at redshift $z = 0$ and constructed the redshift-space distributions of the halo sample by assuming the z -axis as the line of sight.

We use the Cloud-in-cell (Hockney & Eastwood 1981) scheme to calculate the overdensity, δ , on a grid of 256^3 voxels for both the dark matter and halo distributions. We applied a Top-hat smoothing

¹ Downloaded from https://github.com/junkoda/cola_halo

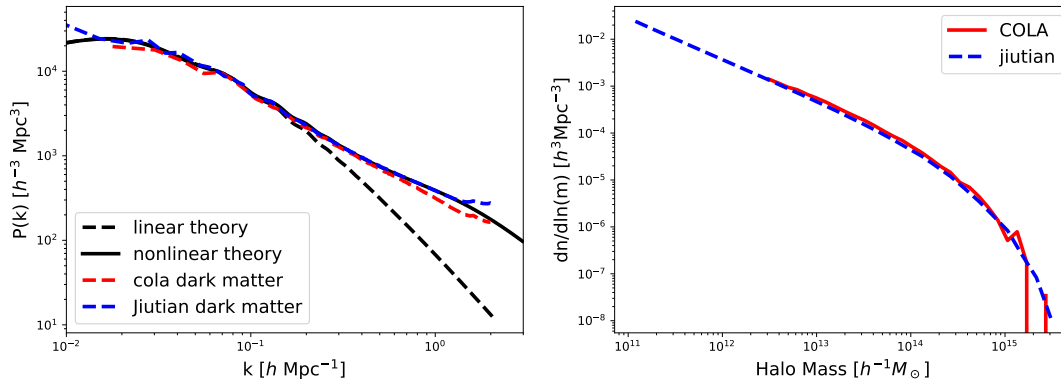


Figure 1. (Left panel) Comparison of the dark matter field’s power spectrum. The red dashed line is shown for the cola simulation with $500 h^{-1}\text{Mpc}$ box size and 512^3 particles. The blue dashed line is for Jiutian simulation with $1000 h^{-1}\text{Mpc}$ box size and 6144^3 particles. Black solid and dashed lines correspond to the non-linear and linear power spectrum, respectively. (Right panel) Comparison of the halo mass function between cola (red solid) and Jiutian (blue dashed).

kernel to the overdensity fields with a smoothing scale of $R_s = 5 h^{-1}\text{Mpc}$. To reduce the variance of the voxel values, we rescaled the overdensity values to lie in the interval $[-1, 1]$ by using the non-linear transformation (Rodríguez et al. 2018): $s(x) = 2x/(x+a) - 1$, where $a = 5$. Each dark matter halo is assigned a mass weight in order to determine the halo density field. We split the dataset into 15 training, 5 validation, and 10 test samples.

In order to verify the generality of our results, we also use a high-resolution N-body simulation, **Jiutian**, as another test sample. This simulation was carried out at the High-Performance Computing Center at Kunshan and was run with L-GADGET, a memory-optimized version of GADGET2 (Springel 2005). Jiutian describes the distribution of 6144^3 dark matter particles in a periodic box of $1000 h^{-1}\text{Mpc}$. The cosmological parameters adopted by this simulation are consistent with the results from **Planck2018** (Planck Collaboration et al. 2020), as well as the COLA simulations. Dark matter halos are identified using the Friends-of-Friends method (Han et al. 2023, in preparation). Figure 1 shows the comparison of the dark matter power spectrum and halo mass function between COLA and Jiutian simulation at redshift $z = 0$. It is quite compatible with the clustering of the dark matter at the median scale, and the distribution of the halo mass above $\log(M) > 12.5 h^{-1}M_\odot$. However, as the limitation of the box size and resolution, the COLA deserved to be distinct from Jiutian on both large and small scales. As a result, one objective of this paper is to test the applicability of the model learned from low-resolution simulation to high-resolution simulation. In order to determine the overdensity field in the Jiutian case, we make a grid of 512^3 voxels and divide it into 8 small grids each with 256^3 voxels. Similarly to the COLA simulation, we also apply the smooth and rescale procedure, as well as the halo mass weight strategy.

Additionally, we use the N-body simulation ELUCID (Wang et al. 2016), which has a different cosmology, as a test sample to check the impact of cosmology on our reconstructions. This simulation, carried out in the Center for High-Performance Computing, Shanghai Jiao Tong University, evolves the distribution of 3072^3 dark matter particles in a periodic box of $500 h^{-1}\text{Mpc}$ on a side with L-GADGET. The cosmological parameters adopted by the simulation are consistent with **WMAP5** results with $\Omega_m = 0.258$, $\Omega_\Lambda = 0.742$, $h = 0.72$, and $\sigma_8 = 0.80$. We construct the overdensity field for dark matter particles and halos in the same scheme as the COLA samples.

3 NEURAL NETWORK

We adapt our network architecture following the UNet style (Ronneberger et al. 2015) and modify its design in accordance with the Pix2Pix generator (Isola et al. 2016). Figure 2 shows the UNet architecture used in this paper, as an encoder-decoder model for image translation where skip connections are used to connect layers in the encoder with corresponding layers in the decoder. The encoder part is comprised of 7 convolutional layers to downsample the input cube to a bottleneck, where the feature cube has a size of 1^3 voxels with 512 channels. The decoder part then reads the bottleneck output and uses 7 transpose convolutional layers to upsample to the required output cube size. As indicated in Figure 2, each layer in the encoder uses blocks of Convolution-BatchNorm-LeakyRelu, whereas those in the decoder use blocks of Convolution-BatchNorm-Dropout-ReLU with a dropout rate of 50%. All convolutional layers use a filter size of $4 \times 4 \times 4$ and a stride of $2 \times 2 \times 2$. Specifically, skip connections are added between the layers with the same sized feature maps so that the first downsampling layer is connected with the last upsampling layer, the second downsampling layer is connected with the second last upsampling layer, and so on. The bottleneck layer, the last layer of the encoder, uses a ReLU activation instead of LeakyRelu by removing batch normalization. After the last layer in the decoder, a convolution is applied to map to the output with one channel, followed by a Tanh function. As an exception to the above notation, BatchNorm is not applied to the first layer in the encoder. All ReLUs in the encoder, with a slope of 0.2, are leaky whereas ReLUs in the decoder are not.

Moreover, we tested the full architectures of the Pix2Pix with an additional discriminator, which is trained to do as well as possible at detecting the generator’s “fakes”. This architecture’s benefit may be a superior ability to forecast small-scale structure (Isola et al. 2016). However, in actual use, Pix2Pix as a generative adversarial network experiences mode collapse, a typical problem that complicates and increases the likelihood of training failure (Farnia & Ozdaglar 2020). In this work, we’ll demonstrate how an architecture using only the Pix2Pix generator from Figure 2 might nonetheless produce a trustworthy outcome on a modest scale.

To train the networks, we use the mean absolute error as the loss function,

$$\mathcal{L}(\delta_p, \delta_t) = \mathbb{E}[|\delta_p - \delta_t|], \quad (1)$$

where δ_p denotes the predicted density field and δ_t denotes the sim-

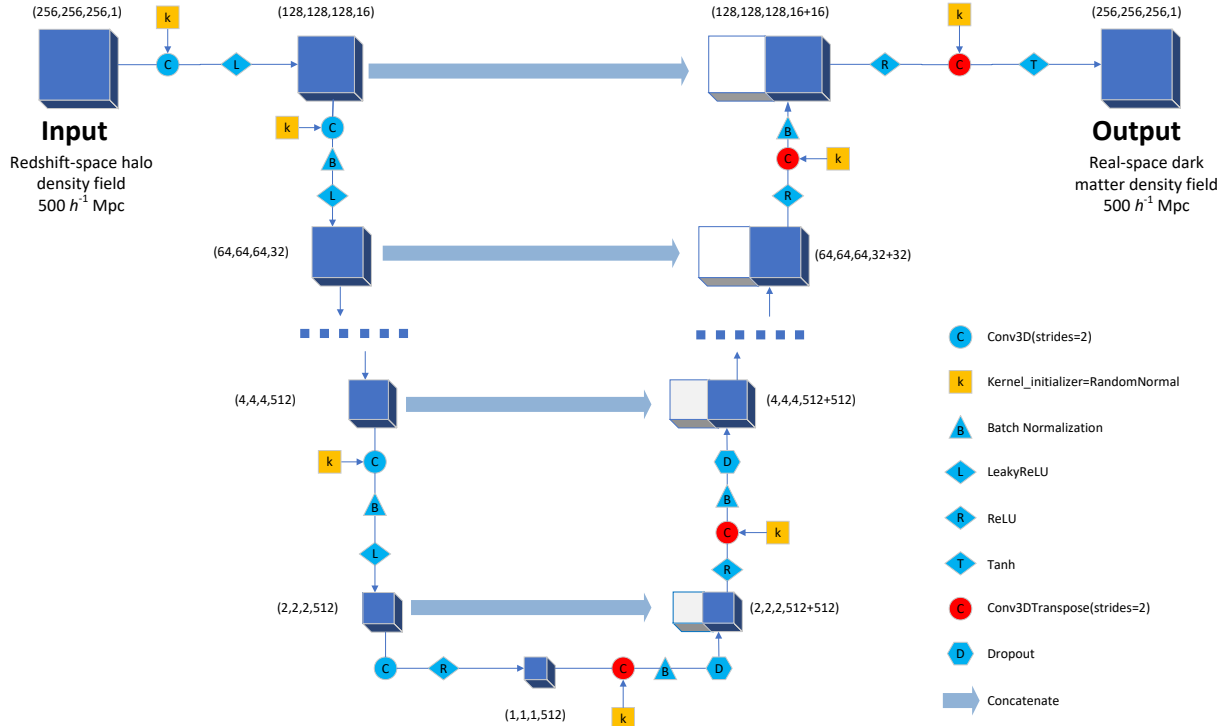


Figure 2. The 3D UNet architecture. Cubes represent 3D feature maps, which have the size of the cubes and the number of channels in each layer indicated. The input and output cube, both of which have 256^3 voxels with $500 h^{-1} \text{Mpc}$ in size, correspond to the redshift-space density field of halo and the real-space density field of dark matter, respectively. The encoder part is comprised of 7 convolutional layers to downsample the input cube to a bottleneck, while the decoder part then reads the bottleneck output and uses 7 transpose convolutional layers to upsample to the output cube. Each layer in the encoder uses blocks of Convolution-BatchNorm-LeakyRelu, whereas those in the decoder use blocks of Convolution-BatchNorm-Dropout-ReLU with a dropout rate of 50%. For clarity, we only show the blocks for the first and last layers in the encoder and decoder. Different symbols represent several calculations, as shown in the lower-right corner.

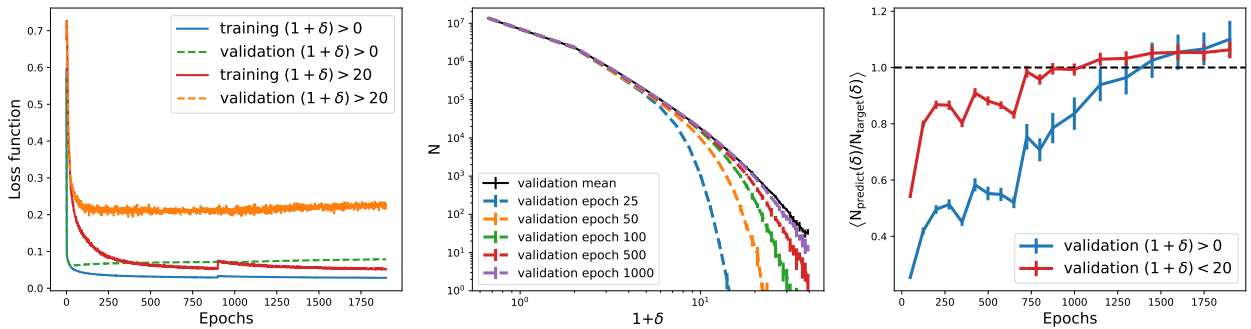


Figure 3. (Left panel) Evolution of the loss function. The blue solid and green dashed lines correspond to the loss functions from the training and validation samples respectively, which are derived from all the voxels with $(1 + \delta) > 0$. The loss functions derived from the voxels that had $(1 + \delta) > 20$ are also provided for the training (red solid) and the validation (orange dashed) samples. (Middle panel) Comparison of the density distribution for the validation samples. The y-axis counts the number of voxels in each $1 + \delta$ bin. The black solid line is shown for the result averaged from the 5 validation samples. Different color lines correspond to the predicted fields in epochs 25, 50, 100, 500, and 1000, as indicated. The error bars indicate the variance among the 5 validation samples. (Right panel) The averaged ratios of the density distribution between prediction and target as a function of epochs. The blue and red lines correspond to the validation-set results from the voxels with $(1 + \delta) > 0$ and those with $(1 + \delta) < 20$, respectively.

ulation target. We train the networks from scratch and initialized the weights from a Gaussian distribution with a mean and standard deviation of 0 and 0.02, respectively. The network sees 15 training samples each epoch, followed by 5 validation samples that are used only for evaluating the models during the training.

In the left panel of Figure 3, we show the evolution of the loss function over a period of 1900 epochs. The blue solid and green dashed lines correspond to the loss functions from the training and validation samples respectively, which are derived from all the voxels with $(1 + \delta) > 0$. Additionally, the loss functions derived from the

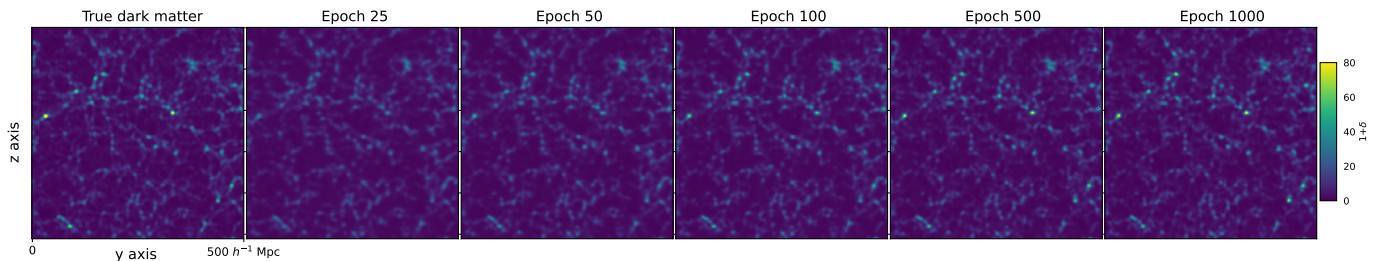


Figure 4. Comparisons of the projected density field distributions in a slice of $500 \times 500 \times 9.76 h^{-1} \text{Mpc}$ for one validation sample. The first panel shows the true dark matter density fields taken from the original simulation. The other five panels correspond to the predictions at epochs 25, 50, 100, 500, and 1000.

voxels that have $(1 + \delta) > 20$ are also provided for the training (red solid) and the validation (orange dashed). It demonstrates that the all-voxel loss function of the validation set is converged after about 50 epochs. However, one can see that the loss function of the validation set keeps decreasing after epoch 50 and is converged after about 250 epochs in the case with $(1 + \delta) > 20$. This demonstrates that the all-voxel loss function, whose values are dominated by large amounts of small densities, makes it difficult to evaluate the training performance of the high-density regions. For instance, only 0.02 percent of the total voxels are those with $(1 + \delta) > 20$. As an illustration, Figure 4 shows the comparisons of the projected density field distributions in a slice of $500 \times 500 \times 9.76 h^{-1} \text{Mpc}$ for one validation sample. The first panel shows the true dark matter density fields taken from the original simulation. The other five panels correspond to the predictions at epochs 25, 50, 100, 500, and 1000. Although it is comparable to the target on a large scale, the prediction at epoch 25 cannot present the high-density region, such as the cluster structure. The high-density structure is increasingly apparent at later epochs and the prediction produced at epoch 1000 performs much better than that made at earlier epochs. Therefore, the networks can still learn effectively even at the convergence stage of the all-voxel loss function.

In this case, we compare the density distribution of the validation samples between the targeted field and the predicted fields at epochs 25, 50, 100, 500, and 1000, as shown in the middle panel of Figure 3. It is evident that from epoch 25 to epoch 1000, there are smaller disparities at the $(1 + \delta) > 20$ between predictions and target, indicating the recovery of high-density voxels has significantly improved. However, as training processes, it appears that the predictions have unreasonably high density. In the right panel of Figure 3, we show the averaged ratios of the density distribution between predictions and target as a function of epochs. The blue and red lines correspond to the validation-set results from the voxels with $(1 + \delta) > 0$ and those with $(1 + \delta) < 20$, respectively. Although the ratios reach unity at about epoch 1300 in the all-voxel case, a significant fraction of voxels with $(1 + \delta) < 20$ have ratios higher than unity. We tested that it would result in an excessive clustering in the density field using the model saved in this stage. Therefore, considering the voxels with $(1 + \delta) < 20$, we select the model as our best model based on the validation-set ratios that were closest to unity between epochs 600 and 1000.

After completing the training, we verify the resulting model with the test samples from COLA fast simulations, Jiutian, and ELUCID N-body simulation, as described in Section 2.

4 VALIDATION WITH COLA TEST SAMPLES

In this section, we test the accuracy and reliability of our resulting model by using the 10 test samples from COLA simulations.

4.1 Pixel-to-pixel comparison

We start with a visual comparison based on the projected density field distribution in a slice of $500 \times 500 \times 9.76 h^{-1} \text{Mpc}$, as shown in Figure 5. The first row shows 5 slices of the true dark matter density fields randomly taken from the COLA test samples. The second row shows the corresponding reconstructed dark matter field based on the resulting UNet model. A comparison with the true fields shows that the reconstruction is generally very successful over the different scales. The reconstructed density fields exhibit recognizable, large-scale structures including clusters, filaments, and voids. It also shows that the model is generally resistant to the boundary effect given that the structure is effectively recovered at the box's border. However, the high-density voxels in the reconstructions, such as the regions around clusters, can be seen to differ slightly from the target, revealing that the models are not perfect.

The left panel of Figure 6 shows the density-density relation between the reconstructed density field $1 + \delta_{\text{rec}}$ and the true field $1 + \delta_{\text{true}}$. The relation is shown for Sample 1 (as illustrated in Figure 5), which is similar to other samples. The three contours encompass 67%, 95%, and 99% of the grid cells in the reconstruction volume. The dashed lines indicate the perfect relation. One sees that the reconstructed field follows the true field without significant bias. The right panel of Figure 6 shows the comparisons of the voxel number distributions. The back and blue lines correspond to the true and the reconstructed density fields, respectively. The error bars show the $\pm 1\sigma$ variance among the 10 test samples. The reconstruction shows a general agreement with the true field at the 1σ level. The performance of the reconstruction in the high-density regions should be limited by the small number of massive halos in the training samples, making it difficult to learn the relationship between the halo and dark matter density field at the cluster regions. Nevertheless, modeling the halo-mass relation at the nonlinear scale, where the halos trace the underlying mass with a more complex bias form, is a promising application for deep learning. We will perform a detailed study on this issue in a subsequent paper.

4.2 Power Spectrum

We now assess the clustering by comparing the power spectrum of the reconstructed dark matter fields with the truth. In the top panel of Figure 7, we show the comparisons of the power spectrum. The black

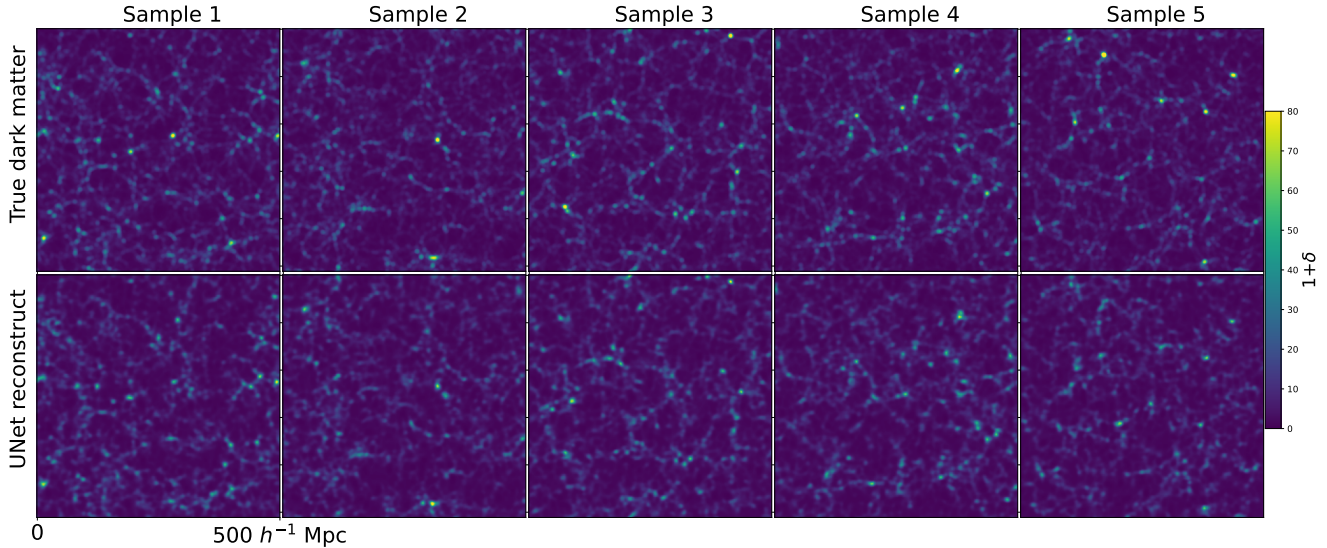


Figure 5. COLA test: Comparisons of the projected density field distribution in a slice of $500 \times 500 \times 9.76 h^{-1} \text{Mpc}$. The first row shows 5 slices of the true dark matter density fields randomly taken from the COLA test samples. The second row shows the corresponding reconstructed dark matter field based on the resulting UNet model.

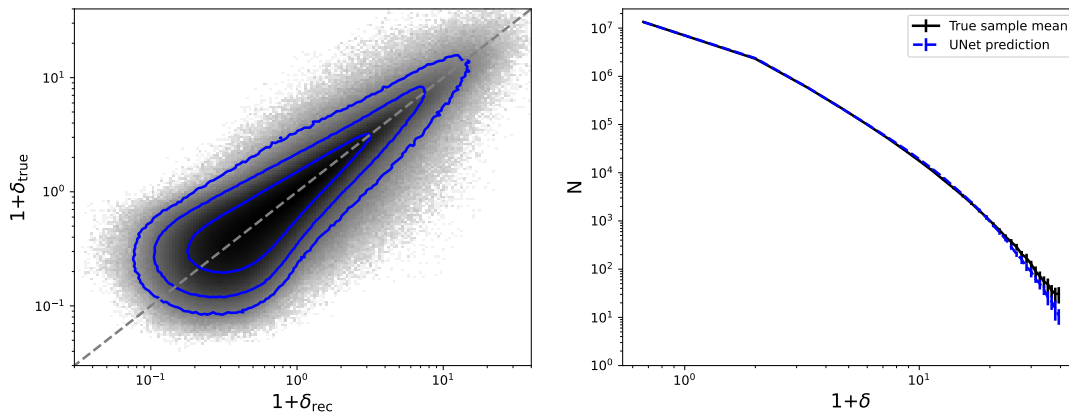


Figure 6. COLA test: (Left panel) Density-density relation between the reconstructed density field $1 + \delta_{\text{rec}}$ and the true field $1 + \delta_{\text{true}}$, for Sample 1 (as indicated in Figure 5). The three contours encompass 67%, 95%, and 99% of the grid cells in the reconstruction volume. The dashed lines indicate the perfect relation. (Right panel) Comparison of the voxel number distributions. The black and blue lines correspond to the true and the reconstructed density fields, respectively. The error bars show the $\pm 1\sigma$ variance among the 10 test samples.

solid and blue dashed lines correspond to the auto-power spectrum of the true and reconstructed fields, respectively. For comparison, the red dot line shows the auto-power spectra of the redshift-space halo field. The bottom panel shows the ratio between the reconstructed and true power spectra, as indicated. The error bars show the $\pm 1\sigma$ variance among the 10 test samples. As shown, the halo's power spectra is biased to that of dark matter. After reconstruction, the resulting auto-power spectra matches the target at the 1σ level over the range of scales $k < 0.3 h \text{Mpc}^{-1}$.

However, even if the power spectra are perfectly reproduced, it is not equivalent to demonstrate that the reconstructions are well performed. In the sense of two independent COLA simulations, they do have very similar power spectra, while their phase space infor-

mation is significantly different. In order to check the concordance between the reconstructed and the true density field, we validate the cross-correlation power spectrum, which is referred to as the phase correlation in Wang et al. (2013). In Figure 7, the green dashed-dot line represents the cross-power spectra of the true and reconstructed fields and the ratios of the reconstructed cross-power spectra to the true one. It is reassuring that the ratios match excellently with the unity within the 1σ range at scales $k < 0.1 h \text{Mpc}^{-1}$. On smaller scales $0.1 < k < 0.3 h \text{Mpc}^{-1}$, it reveals the value of ratios less than unity. Overall, the reduction of the cross-correlation power spectrum at $k = 0.1$ and $0.3 h \text{Mpc}^{-1}$ are at 1% and 10% levels, respectively.

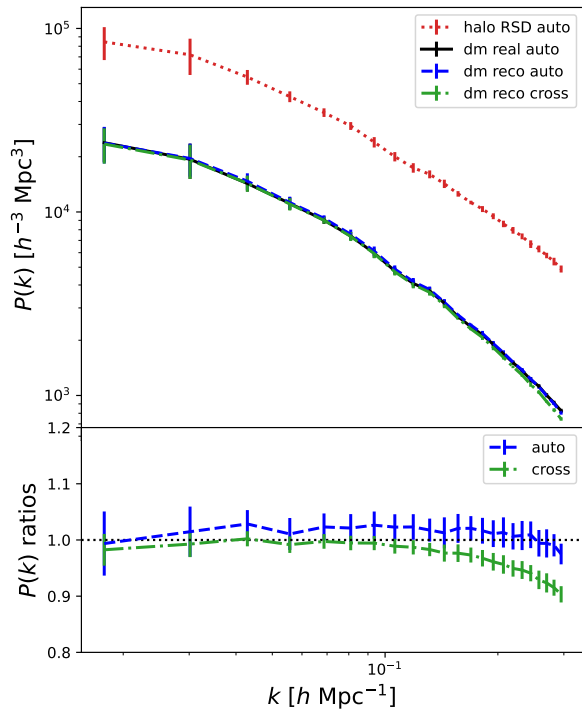


Figure 7. COLA test: Comparison of the power spectrum with ratios. The black solid and blue dashed lines correspond to the auto-power spectrum of the true and reconstructed fields, respectively. The green dashed line is shown for the cross-power spectra of the true and reconstructed field. As a comparison, the red dashed line is shown for the auto-power spectra of the halo field in redshift space. The bottom panel shows the ratio between the reconstructed and true power spectra, as indicated.

4.3 Quadrupole

In order to gauge the accuracy of the correction of the redshift-space distortions, we now compare the 2D power spectra, $P(k_{\perp}, k_{\parallel})$, of the reconstructed dark matter field with the truth, shown in the left panel of Figure 8. Gray-band and blue-dashed contours correspond to the true and reconstructed field, respectively. The red dot contours represent the redshift-space halo's $P(k_{\perp}, k_{\parallel})$ with a factor $1/b^2$, where b is the bias factor of halos. Note that the results are averaged from the 10 test samples. The redshift-space $P(k_{\perp}, k_{\parallel})$ is clearly anisotropic with the "elongated" feature in the central region, revealing the impact of the Kaiser effect on large scales (small k values). After reconstruction, the resulting $P(k_{\perp}, k_{\parallel})$ is clearly more isotropic and perfectly round on large scales. A comparison with the true $P(k_{\perp}, k_{\parallel})$ shows that the correction for the RSDs is overall very successful.

The right panel of Figure 8 compares the quadrupole, $P_2(k)$. Back and blue-dashed lines correspond to the true and reconstructed $P_2(k)$, respectively. Error bars indicate the variance among the 10 test samples. The red dot line shows the result of the redshift-space halo. In redshift space, the Kaiser effect causes the quadrupole to deviate significantly from zero. In the true field without RSDs, we expect isotropy to result in a quadrupole $P_2(k) = 0$. Hence, if the correction for redshift distortions is successful, the resulting clustering should have a vanishing quadrupole, and thus $P_2(k) = 0$. As shown, in redshift space $P_2(k)$ has large deviations from zero, while in the true field, $P_2(k)$ is very close to zero. In the reconstruction, the

quadrupole is much closer to zero within the error bars over different scales, indicating that the reconstruction has successfully corrected the majority of redshift-space distortions.

Based on the test results, we conclude that our neural network tuned by small sample size is capable of predicting the density field for new data and can accurately correct for RSDs, resulting in reliable clustering dark matter density field. It should be noted that further training sets are still needed to improve the performance at small scales. To make a more accurate reconstruction, it is beneficial to reduce the variance of the model prediction by taking an average from several models saved from the neural network.

5 VALIDATION WITH N-BODY SIMULATIONS

In this section, our goals are to: (i) verify the generality of the UNet model to new sets of samples from the N-body simulation with much larger volume and higher resolution, and (ii) check the impact of cosmology on the reconstruction accuracy. Therefore, we validate the reconstruction with Jiutian and ELUCID N-body simulation data, as mentioned in Section 2. Compared to the COLA training samples, Jiutian has a much larger volume and higher resolution while ELUCID uses distinct cosmological parameters. In order to match the box volume of the COLA training sample, we first divided Jiutian into 8 identically sized boxes before applying the UNet model and afterward concatenated them back to the box in the original volume.

As a visual comparison, Figure 9 shows the projected true density fields (left panels) versus the reconstructed fields (right panels). The upper and lower panels correspond to Jiutian in a slice of $1000 \times 1000 \times 9.76 h^{-1} \text{Mpc}$ and ELUCID in a slice of $500 \times 500 \times 9.76 h^{-1} \text{Mpc}$, respectively. As can be seen, both of the reconstructed density fields show filamentary structures connecting high-density nodes, similar to that in the original field. Figure 10 shows the density-density relations and the comparisons of the density distributions between the reconstructed and the true density field for both Jiutian and ELUCID samples, as indicated. The reconstructed density fields are linearly correlated with the true fields and do not exhibit any significant bias for both cases, which are consistent with the result from the COLA test samples. In the density distribution, the reconstruction matches favorably with the true field at the appreciable range despite an underestimation at large δ , indicating overall success for the reconstruction of both Jiutian and ELUCID samples. Although the reconstructions are systematically underestimated at the range of $1+\delta > 20$, it only takes up 0.02 percent of the total voxels. The performance of the reconstruction could be a consequence of the limited number of massive halos in the training samples, which resulted in poor learning for the halo-matter relation at high-density regions, as discussed in Section 4.1.

Figure 11 shows the comparisons of the power spectrum, $P(k)$, for Jiutian (left panels) and ELUCID (right panels). As indicated, different lines are shown for the auto-correlation and cross-correlation $P(k)$ of the true and the reconstructed dark matter, and the auto-correlation $P(k)$ of redshift-space halos fields. The bottom panels show the ratios between the reconstructed and true power spectrum, as indicated. By considering the cosmic variance due to the limited number of Fourier modes for a finite-volume survey, we estimate the error for the power spectrum in a theoretical way (e.g. Song et al. 2021),

$$\Delta P(k) = \frac{P(k)}{\sqrt{N_k}} \quad (2)$$

where N_k is the number of independent k -modes available per bin.

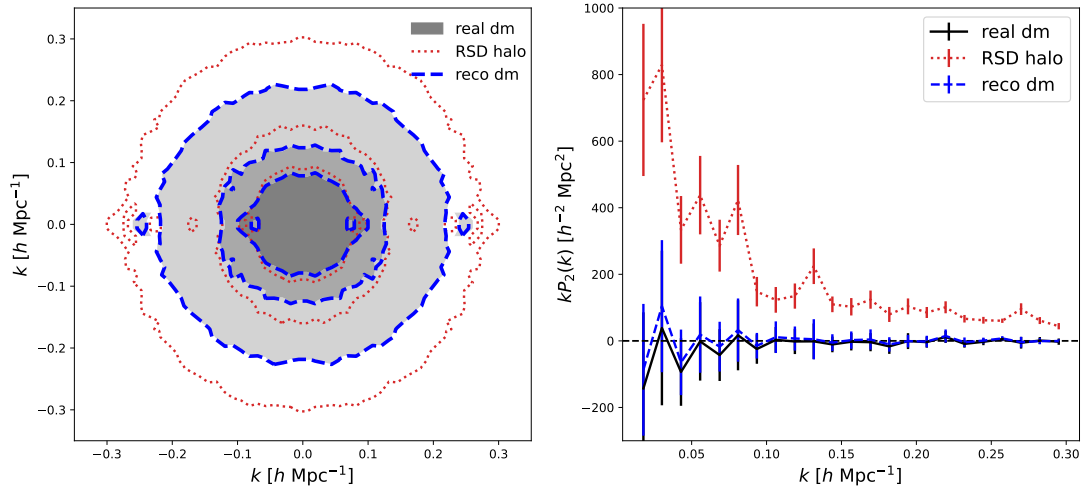


Figure 8. COLA test: (Left panel) Comparison of 2D power spectrum between the reconstructed and the true dark matter field. Gray-band and blue dashed contours correspond to the true and reconstructed field, respectively. The red dot contours represent the redshift-space halo's 2D power spectra with a factor $1/b^2$, where b is the bias factor of halos. Note that the results are averaged from the 10 test samples. (Right panel) Comparison of the quadrupole between the reconstructed (blue dashed) and the true (black solid) density field. The red dot line represents the result of the redshift-space halo.

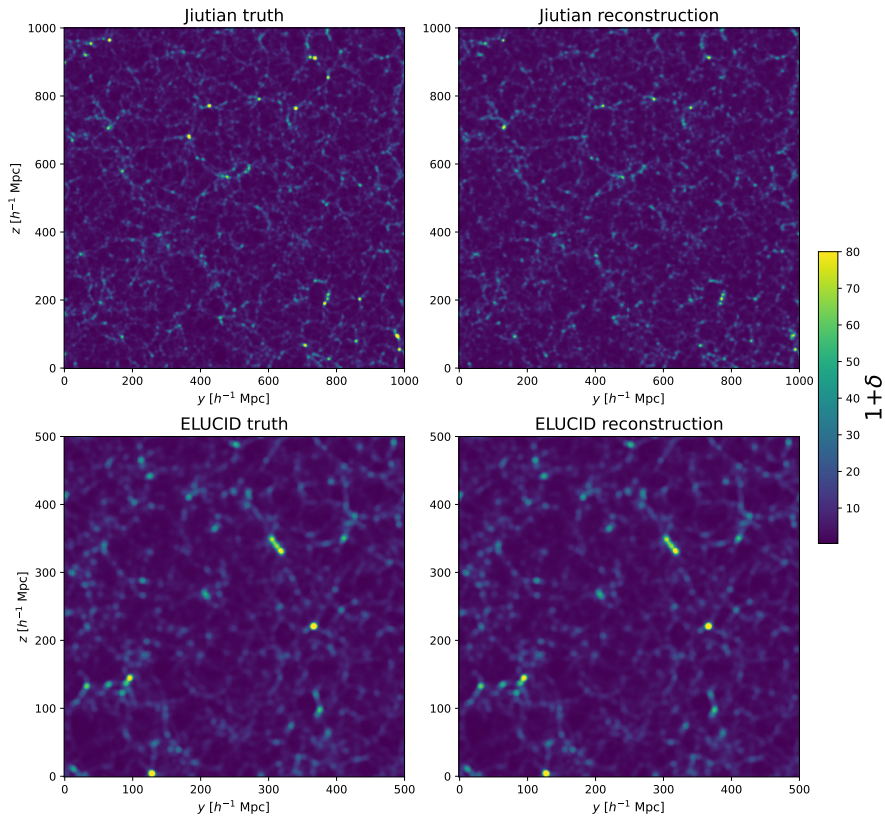


Figure 9. Jiutian and ELUCID test: The projected true density fields (left panels) versus the reconstructed fields (right panels). The upper and lower panels correspond to Jiutian in a slice of $1000 \times 1000 \times 9.76 h^{-1} \text{ Mpc}$ and ELUCID in a slice of $500 \times 500 \times 9.76 h^{-1} \text{ Mpc}$, respectively.

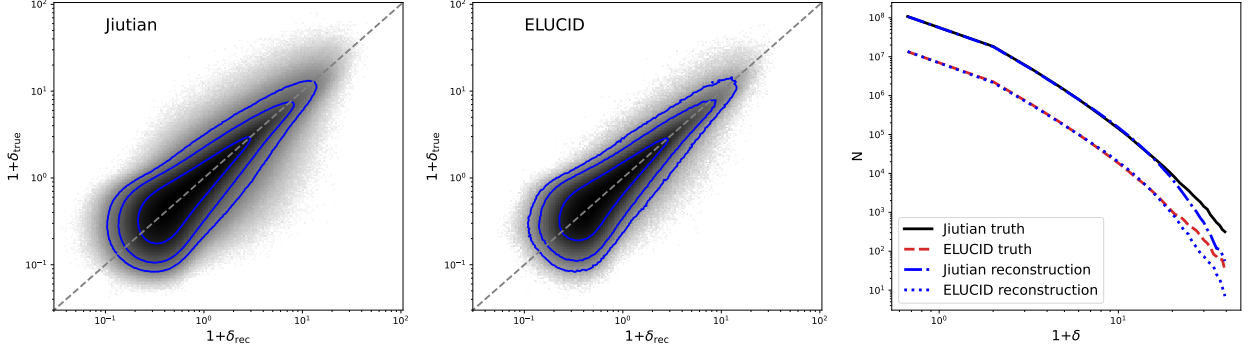


Figure 10. Jiutian and ELUCID test: (Left and middle panels) Density-density relation between the reconstructed density field $1 + \delta_{\text{rec}}$ and the true field $1 + \delta_{\text{true}}$. The three contours encompass 67%, 95%, and 99% of the grid cells in the reconstruction volume. The dashed lines indicate the perfect relation. (Right panel) Comparisons of the voxel number distributions. The back solid and red dashed lines correspond to Jiutian's and ELUCID's true density fields, respectively. The blue dash-dot and dot lines correspond to the reconstruction for Jiutian and ELUCID, respectively.

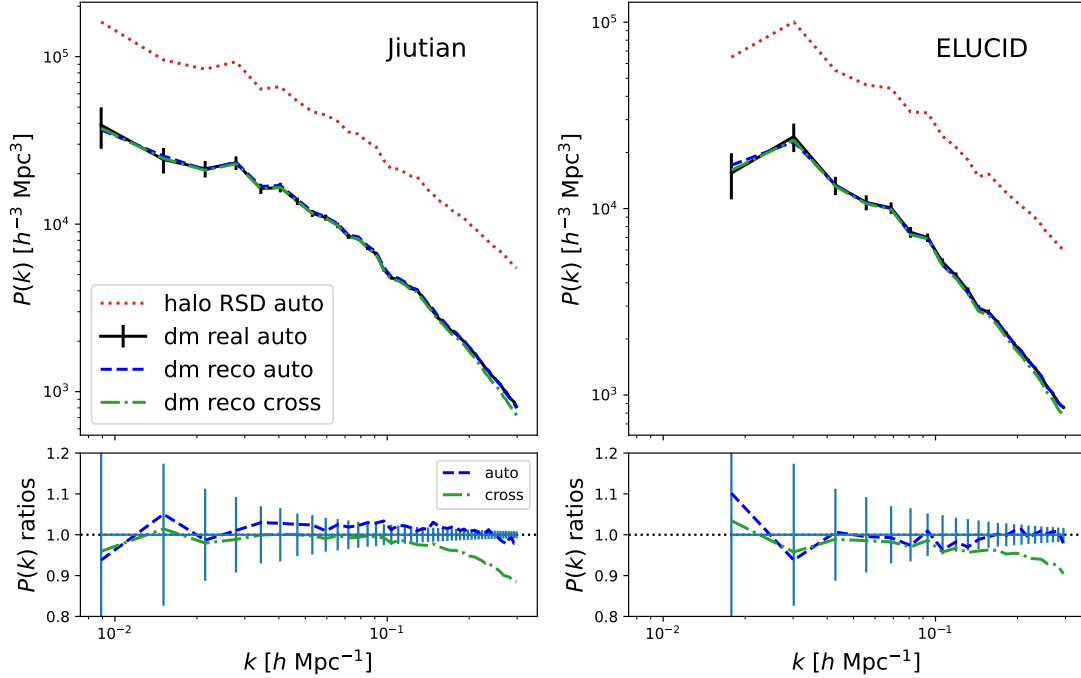


Figure 11. Jiutian and ELUCID test: same as Figure 7 but for Jiutian (left panels) and ELUCID (right panels). The error bars are computed using Equation 2.

Compared to the halos' $P(k)$, the reconstructed auto-correlation $P(k)$ values match the target truths at the 1σ level over the range of scales $k < 0.3 h \text{Mpc}^{-1}$. The cross-correlation $P(k)$ values lie in between the auto power spectrum and the ratios are very close to unity at the 1σ level on a scale of $k < 0.1 h \text{Mpc}^{-1}$. The underestimation at scale $k > 0.1 h \text{Mpc}^{-1}$ should be caused by the inaccurate reconstruction in the high-density region due to the limited number of massive halos in current training samples (see also the discussion in Section 4.1). More importantly, the overall reduction of the cross-correlation power spectrum at $k = 0.1$ and $0.3 h \text{Mpc}^{-1}$ are very similar to COLA testing results, again at 1% and 10% levels, respectively. As a result, we conclude that the reconstructions of the dark

matter power spectrum for the Jiutian and ELUCID simulations are both appreciably accurate and consistent with the COLA test results.

To test the correction for the RSD effect, Figure 12 shows the comparisons of the 2D power spectrum $P(k_{\perp}, k_{\parallel})$ (left panels) and the quadrupole $P_2(k)$ (right panels). The upper and lower panels correspond to Jiutian and ELUCID results, respectively. The black and blue colors are shown for the true and reconstructed density fields, respectively. As a comparison, the red dashed lines represent the redshift-space halo's $P(k_{\perp}, k_{\parallel})$, which, note that, is multiplied by the factor $1/b^2$ (with $b = 1.86$ serving as the halo bias parameter at redshift $z = 0$). Similar to the conclusions based on COLA test samples, the reconstructed $P(k_{\perp}, k_{\parallel})$ values are in very good agree-

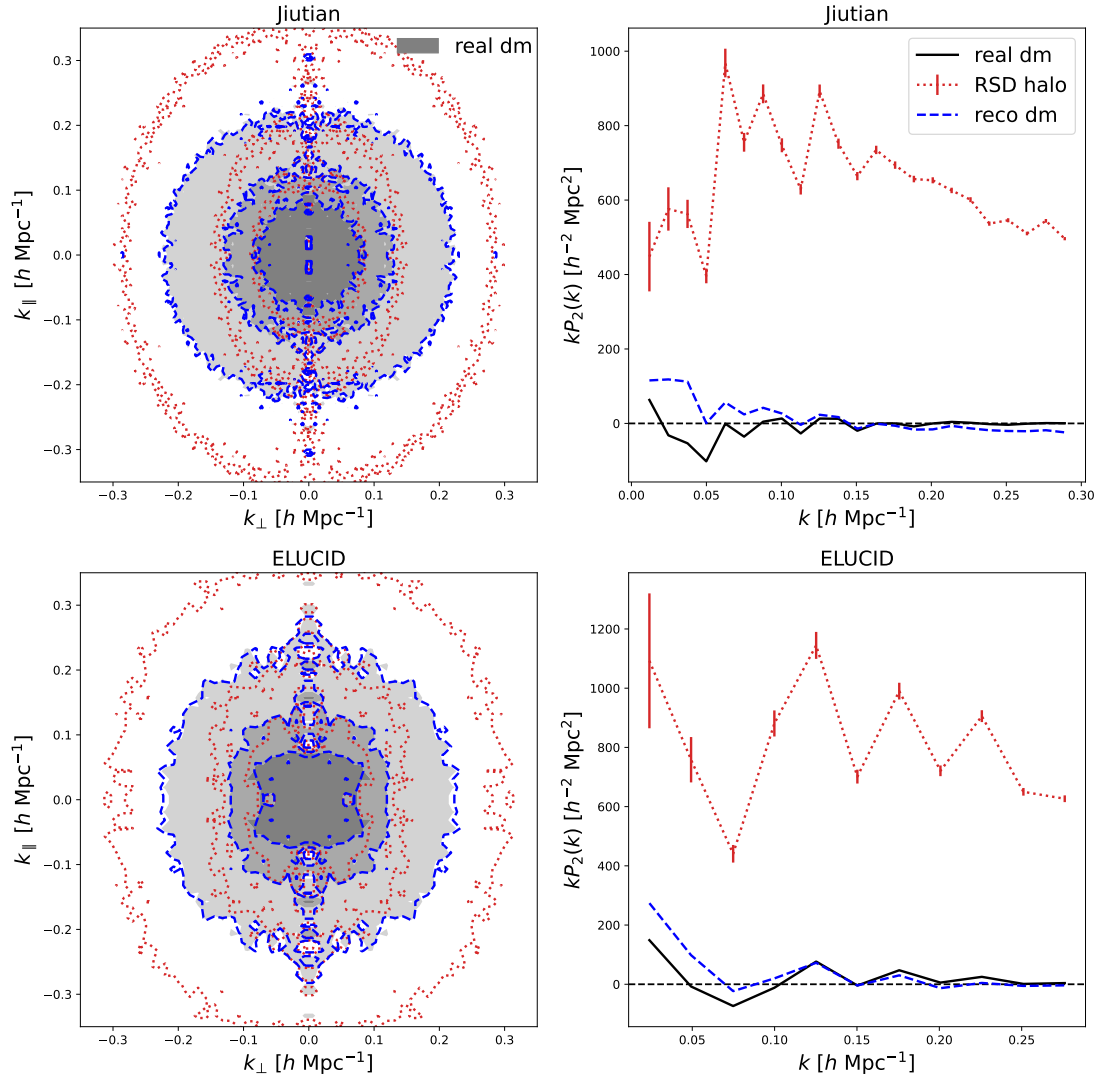


Figure 12. Jiutian and ELUCID test: same as Figure 8 but for Jiutian (upper panels) and ELUCID (lower panels). The error bars for the quadrupole of the redshift-space halo field are computed using Equation 2.

ment with the true $P(k_{\perp}, k_{\parallel})$ and much more isotropic than that of the redshift-space halos. In the quadrupole, as expected, the redshift-space halo's $P_2(k)$ values have considerable deviations from zero, whereas the $P_2(k)$ values for the reconstruction are much closer to zero. Compared with the true $P_2(k)$, the reconstructed $P_2(k)$ values have a modest positive signal on large scales, which is due to noise according to the test in Section 4.3. On smaller scales, the reconstruction shows a somewhat negative $P_2(k)$, which may result from the inaccurate reconstruction in the high-density region. As a result, our UNet-based reconstruction can be able to largely eliminate the RSD effects for both Jiutian and ELUCID samples.

Therefore, we draw a conclusion that the UNet model, which was fine-tuned using COLA training samples of low volume and low resolution, is capable of accurately reconstructing the dark matter field of the N-body simulation even with larger volume and higher resolution. Meanwhile, our reconstruction is unaffected by the different cosmologies between the training sample (**Planck2018**) and the test sample (**WMAP5**).

6 TESTING THE RECONSTRUCTION OF THE VELOCITY AND TIDAL FIELD

We now test the effectiveness of the UNet-based reconstructed density field in recovering the velocity field and the tidal field using the Jiutian sample.

6.1 Reconstructing velocity field

We compute the velocity field from the density field reconstructed by the UNet models. In the linear regime, the peculiar velocities are induced by and proportional to the perturbations in the matter distribution. In Fourier space, we have

$$\mathbf{v}(\mathbf{k}) = H a f(\Omega_m) \frac{i\mathbf{k}}{k^2} \delta(\mathbf{k}), \quad (3)$$

where $H = \dot{a}/a$ is the Hubble parameter, a is the scale factor, $f(\Omega_m) = \Omega_m^{0.55}$ (Linder & Cahn 2007) is the growth factor and $\delta(\mathbf{k})$ is the Fourier transform of the density perturbation field $\delta(\mathbf{x})$. Hence, for a given cosmology one can directly infer the linear ve-

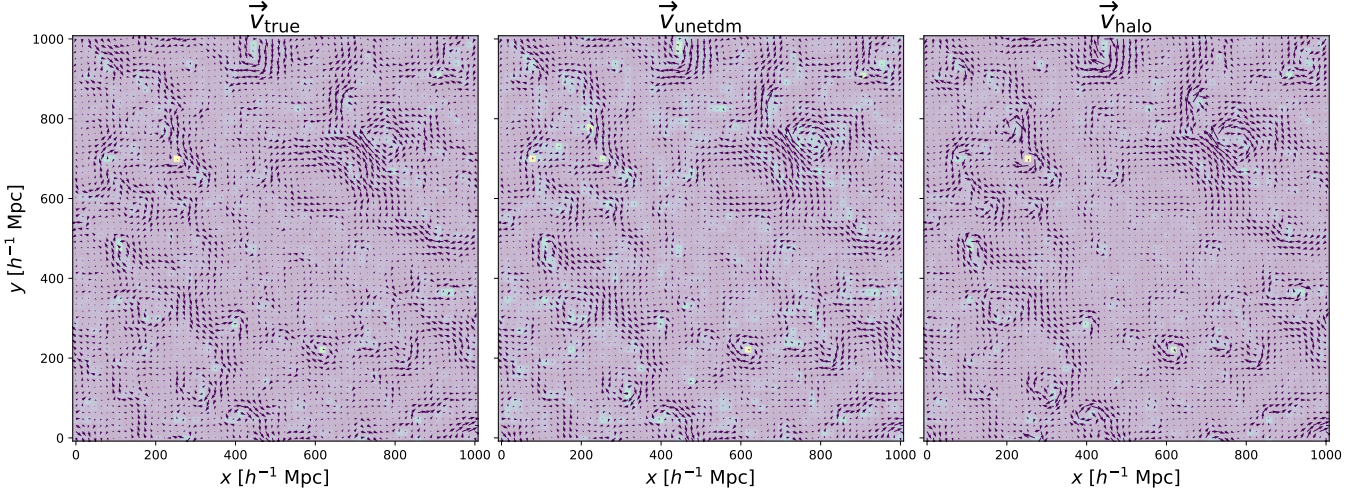


Figure 13. Jiutian test: Velocity fields together with the density fields in a slice of $1000 \times 1000 \times 9.76 h^{-1} \text{Mpc}$. The left panel shows the true field, \vec{v}_{true} , from the original simulation. The middle panel shows the velocity, \vec{v}_{unetdm} , reconstructed from the UNet-reconstructed dark matter density field described in the previous section. The right panel shows the velocity field, \vec{v}_{halo} , reconstructed from the halo density field with a linear bias b_h . The length of an arrow is proportional to the magnitude of the velocity it represents.

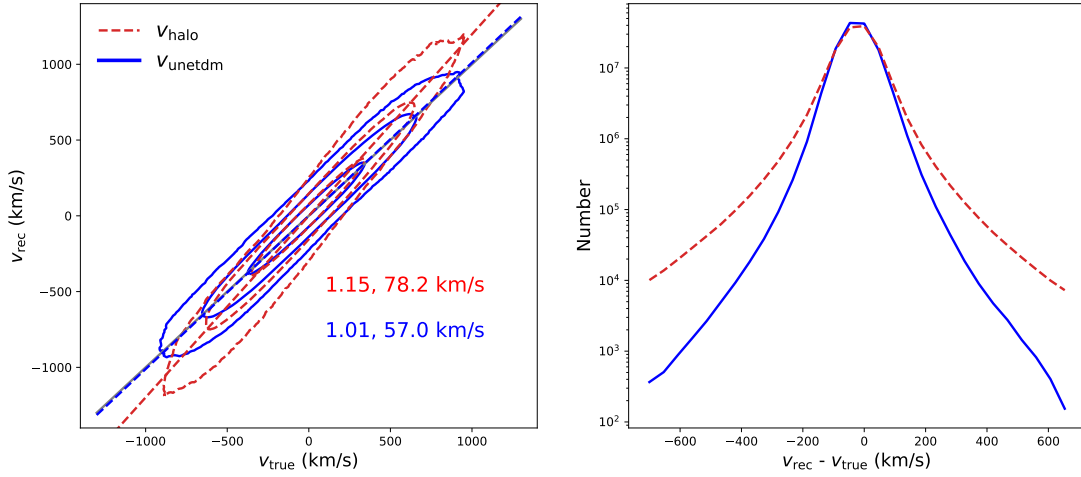


Figure 14. Jiutian test: Comparison of the velocity-velocity relation (left panel) and the number distribution of the difference, $v_{\text{rec}} - v_{\text{true}}$ (right panel). The blue solid and red dashed curves correspond to the results from the Unet-reconstructed density field, v_{unetdm} , and from the halo field, v_{halo} , respectively. Note that all the velocities are along the z-axis. In the left panel, the three contours encompass 67%, 95%, and 99% of the grid cells, and the best-fitting relation of the correlation between reconstruction and the simulation is indicated as the corresponding color dashed line. The gray line indicates the unity slope relationship. The slope of the best-fitting and the scatter, in terms of the RMS in $v_{\text{rec}} - v_{\text{true}}$, are also indicated in the left panel with red for v_{halo} and blue for v_{unetdm} .

locity field from the density perturbation field, $\delta(\mathbf{x})$. In traditional method (eg. Wang et al. 2009), the peculiar velocity field is reconstructed from the halo density field by substituting $\delta(\mathbf{k})$ in Eq. (3) with $\delta_h(\mathbf{k})/b_h$, where δ_h is the dark matter halo density field and b_h is the linear bias parameter for dark matter halos above some mass threshold. In this case, the distribution of halos is considered to be a point set that represents the underlying mass distribution with a local bias. However, the point set of halos may not be a local sampling of the underlying mass density field, as the likelihood of a halo at a particular location may depend on the presence of other dark matter

particles at or near this location (Mo et al. 2010). In this case, the nonlinear velocity field at small scales may not be predicted by the linear-bias method. On the other hand, although Wang et al. (2009) proposed a method to predict the peculiar velocities using the reconstructed density field, it is quite time-consuming as they have to correct for the positions of the redshift-space halos and iterate until convergence is achieved. In this paper, we have successfully reconstructed the density field by correcting for the RSD effects and can directly rebuild the velocity field using Eq. (3) without making any assumptions about the linear bias.

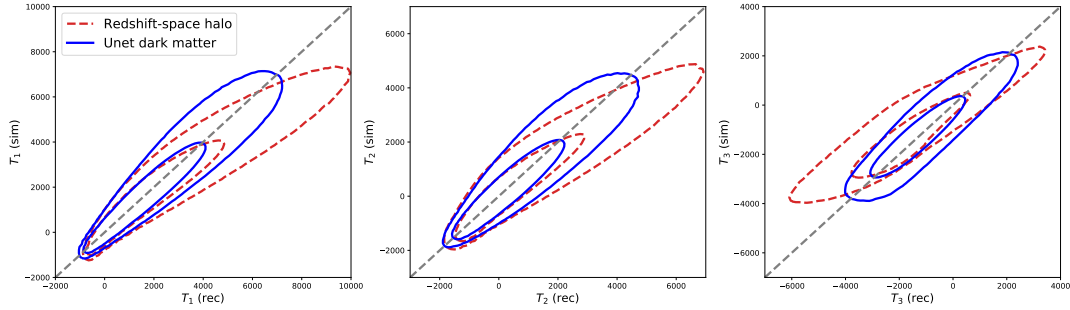


Figure 15. Jiutian test: The eigenvalues of the reconstructed tidal tensor, versus those from the true dark matter field of the Jiutian simulation. Red and blue contours correspond to the values from the UNet-reconstructed dark matter field and the redshift-space field of halos. The contours for each result encompass 90 and 99 percent of the grid cells.

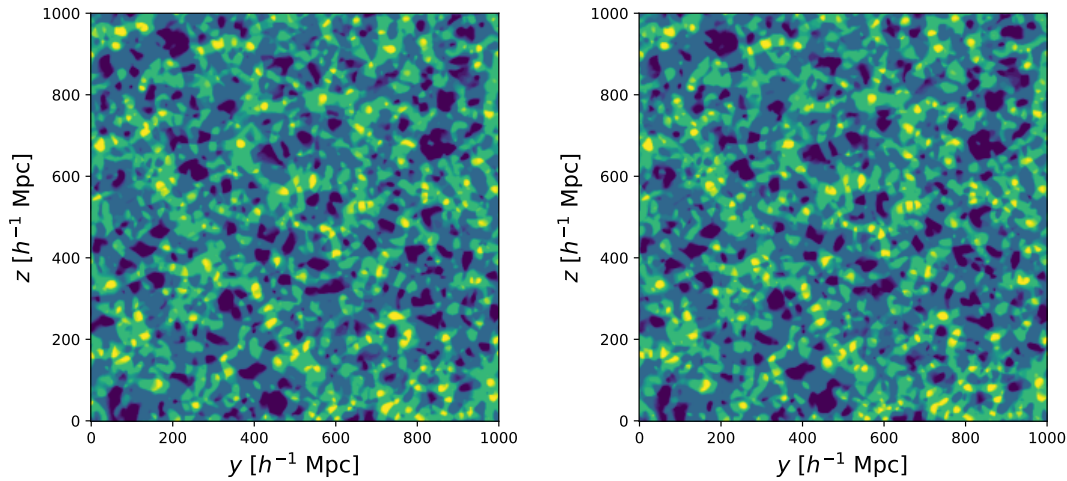


Figure 16. Jiutian test: Comparison of the classification of the large-scale structure between the true dark matter field (left panel) and the UNet-reconstructed field (right panel) in a slice of $1000 \times 1000 \times 9.76 h^{-1} \text{Mpc}$. The yellow, yellow-green, green, and black regions are grid cells located at structures classified as cluster, filament, sheet, and void, respectively.

In Figure 13, we show the velocity fields together with the density fields in a slice of $1000 \times 1000 \times 9.76 h^{-1} \text{Mpc}$. The left panel shows the true field, \vec{v}_{true} , from the original simulation, while the middle panel shows the reconstructed velocity, \vec{v}_{unetdm} , which was derived from the UNet-reconstructed density field. For comparison, the right panel shows the velocity field, \vec{v}_{halo} , which was derived from the halo density field with the linear bias b_h . In order to avoid having to iteratively correct for RSD effects, we compute \vec{v}_{halo} from the halo density field in real space rather than redshift space, whereas \vec{v}_{unetdm} is computed from the UNet-based reconstructed density field that is recovered from the redshift-space halo density field. In the figures, the length of an arrow is proportional to the magnitude of the velocity it represents. In a case when density is low, both reconstructions perform well. Nevertheless, the velocities \vec{v}_{halo} appear to be significantly noisier in the high-density region, such as the area around $(x, y) = (220, 700)$. This is a manifestation of inaccurate for grid cells where non-local bias effects are not negligible. Instead, it is clear that the velocities \vec{v}_{unetdm} maintain to closely follow the true velocities even in the high-density area.

In Figure 14, we show the velocity-velocity relation (left panel) and the distribution of the velocity difference (right panel) between

the reconstruction and the truth, $v_{\text{rec}} - v_{\text{true}}$. The blue solid and red dashed contours correspond to the reconstructed velocity v_{unetdm} and v_{halo} , respectively. The three contours encompass 67%, 95%, and 99% of the grid cells. Here, we simply compare the z-component of the velocities because the RSD effects are assumed to be along the z-axis, and the results for all three directions are rather comparable. We performed a linear regression and the best-fitting lines are shown in the figure as the blue and red dashed lines for both cases. The value of the slope and the scatter, in terms of the RMS in $v_{\text{rec}} - v_{\text{true}}$, are also given in the panel. The velocity v_{unetdm} is linearly correlated with the true velocity with a best-fitting slope of 1.01, while for the velocity v_{halo} , the best-fitting slope of the correlation (1.15) deviates significantly from unity. For the distributions of $v_{\text{rec}} - v_{\text{true}}$, both reconstructed velocities peak nicely at zero but the scatter (78.2 km/s) of $v_{\text{halo}} - v_{\text{true}}$ is 37.2 percent larger than that (57 km/s) of $v_{\text{unetdm}} - v_{\text{true}}$. It should be noted that the velocity v_{halo} is rebuilt without including the error introduced by the RSD effects. Based on these results, we conclude that the UNet-reconstructed dark matter field can be reliably used to reproduce the cosmic velocity field and outperforms the halo-based reconstruction.

6.2 Reconstructing tidal field

We now move to the reconstruction of the large-scale tidal field through the tidal tensor, T_{ij} , defined as,

$$T_{ij} = \frac{\partial^2 \phi}{\partial x_i \partial x_j}, \quad (4)$$

where i and j are indices with values of 1, 2, or 3, and ϕ is the peculiar gravitational potential which can be calculated from the mass density field through the Poisson equation,

$$\nabla^2 \phi = 4\pi G \bar{\rho} \delta, \quad (5)$$

where $\bar{\rho}$ is the average density of the universe. Subsequently, the tidal tensor is diagonalized to obtain the eigenvalues $\lambda_1 \geq \lambda_2 \geq \lambda_3$ of the tidal tensor at each grid point.

Figure 15 shows the eigenvalues of the tidal field reconstructed from the UNet dark matter field, versus the tidal field calculated directly from the true dark matter field of the Jiutian simulation. Overall, the eigenvalues of the reconstructed tidal tensor are strongly correlated with that based on the true dark matter field. For comparison, we also present the results using the method from Wang et al. (2009), which calculates the peculiar gravitational potential from the distribution of dark matter halos with a linear bias in Equation 6.2. It shows clearly that the reconstruction based on halo data has a significant bias and a slightly larger scatter. This is a consequence of the inaccurate linear bias on small scale. As we adopt the UNet-reconstructed dark matter field, the bias between the reconstructed and target tidal fields is nearly nonexistent, and the scatter decreases as well.

The eigenvalues of the tidal field can be used to define the morphologies of large-scale structures in one of four classes:

- cluster: a grid cell with three positive eigenvalues;
- filament: a grid cell with one negative and two positive eigenvalues;
- sheet: a grid cell with two negative and one positive eigenvalue;
- void: a grid cell with three negative eigenvalues.

Figure 16 shows the classification of the large-scale structure in Jiutian simulation, based on the true dark matter field (left panel), versus the UNet field (right panel). It shows two of them are quite consistent and nicely in accord with the CDM scenario of structure formation. The yellow-green grid cells clearly show the filamentary structure that connects the yellow grid cells, which are referred to as clusters, whilst the green cells are sheets with more diffused structures enclosing the yellow-green cells. Black areas can also be seen as void cells.

7 SUMMARY AND CONCLUSION

In this study, we build a deep neural network to reconstruct the underlying mass distribution from the distribution of halos in redshift space. Our reconstruction starts with dark matter halos, which is motivated by the fact that galaxy groups can be used to represent the dark halo population and can be well-defined with halo mass from large redshift surveys of galaxies. With the 256^3 -voxel density field map as an input, we implement a UNet-style neural network with 7 convolutional layers and 7 transpose convolutional layers where skip connections are used. We trained the UNet-style neural network using the COLA simulation, which is an approximation of the N-body simulation. We save the best model at the optimum phase after an in-depth evaluation of the training process.

We first validate the resulting UNet model using 10 COLA testing samples, which have the same 512^3 particles and $500 h^{-1} \text{Mpc}$ box size as the training samples. By conducting a series of comparison tests, including density-density relation, density distribution, auto-correlation, cross-correlation, quadrupole, and 2D power spectrum, we find that the UNet model can reasonably recover the dark matter density fields and accurately correct for RSDs. Overall, the reconstructed dark matter matches the target truth with only 1% and 10% reduction of the cross-correlation power spectrum at $k = 0.1 h \text{Mpc}^{-1}$ and $0.3 h \text{Mpc}^{-1}$, respectively.

We further verify the resulting UNet model using the Jiutian simulation, which is a typical N-body simulation with 6144^3 particles in a $1000 h^{-1} \text{Mpc}$ -size box, and the ELUCID N-body simulation, which has a different cosmology of **WMAP5**. As a result, the dark matter density field can be recovered consistently at the same accuracy level and the RSD effects can be effectively eliminated for both Jiutian and ELUCID samples. Therefore, the UNet model, which was fine-tuned using the COLA small-volume and low-resolution training samples, is capable of accurately reconstructing the dark matter field of the N-body simulation even with larger volume and higher resolution. Meanwhile, our reconstruction is unaffected by the different cosmologies between the training sample (**Planck2018**) and the test sample (**WMAP5**).

At last, we test the effectiveness of the UNet-based reconstructed density field in recovering the velocity field and the tidal field using the Jiutian simulation data. We have our results as follows.

- The reconstructed velocity field from the UNet-reconstructed density field is linearly correlated with the true velocity field with a slope of 1.01, and the distributions of $v_{\text{rec}} - v_{\text{true}}$ peak nicely at zero with an RMS error of 57 km/s. In comparison, the velocities reconstructed from the halo density field (with a linear halo bias) exhibit a considerable bias with a slope of 1.15 and a 37.2 percent larger scatter.
- The tidal field derived from the UNet-reconstructed density field is unbiased compared to that computed from the true dark matter, whereas the reconstructed tidal field from halo data has a significant bias. The eigenvalues of the UNet-based reconstructed tidal field can exhibit recognizable, large-scale structures including clusters, filaments, sheets, and voids that are consistent with those based on the true dark matter field.

As a result, the UNet-based model can reliably reproduce the cosmic density field and generalizes to the high-resolution N-body simulation after being trained with low-resolution COLA simulations. This shortens the computation time for producing training data and enhances the deep learning method's applicability to enormous amounts of data from large galaxy surveys. Furthermore, it is clear that the deep learning approach outperforms the traditional approach based on the linear bias model and is useful in precisely recovering the velocity field and tidal field of dark matter. This paper only serves as a proof-of-concept, and the applications of the method to actual data will be presented in forthcoming papers.

ACKNOWLEDGEMENTS

This work is supported by the National Natural Science Foundation of China (Nos.12103037, 11833005, 11890692), 111 project No. B20019, and Shanghai Natural Science Foundation, grant No. 19ZR1466800. We acknowledge the science research grants from the China Manned Space Project with No. CMS-CSST-2021-A02.

This work is supported by High-Performance Computing Platform of Xidian University.

REFERENCES

- Akeson R., et al., 2019, *arXiv e-prints*, p. [arXiv:1902.05569](#)
- Aragon-Calvo M. A., 2019, *MNRAS*, **484**, 5771
- Avila-Reese V., Colín P., González-Samaniego A., Valenzuela O., Firmani C., Velázquez H., Ceverino D., 2011, *ApJ*, **736**, 134
- Berger P., Stein G., 2019, *MNRAS*, **482**, 2861
- Brown M. J. I., et al., 2008, *ApJ*, **682**, 937
- Cacciato M., van den Bosch F. C., More S., Li R., Mo H. J., Yang X., 2009, *MNRAS*, **394**, 929
- Colless M., et al., 2001, *MNRAS*, **328**, 1039
- Crocce M., Pueblas S., Scoccimarro R., 2006, *MNRAS*, **373**, 369
- DESI Collaboration et al., 2016a, *arXiv e-prints*, p. [arXiv:1611.00036](#)
- DESI Collaboration et al., 2016b, *arXiv e-prints*, p. [arXiv:1611.00037](#)
- Davis M., Peebles P. J. E., 1983, *ApJ*, **267**, 465
- Davis M., Efstathiou G., Frenk C. S., White S. D. M., 1985, *ApJ*, **292**, 371
- Erdoğan P., et al., 2004, *MNRAS*, **352**, 939
- Farnia F., Ozdaglar A., 2020, *arXiv e-prints*, p. [arXiv:2002.09124](#)
- Fisher K. B., Davis M., Strauss M. A., Yahil A., Huchra J. P., 1994, *MNRAS*, **267**, 927
- Fisher K. B., Lahav O., Hoffman Y., Lynden-Bell D., Zaroubi S., 1995, *MNRAS*, **272**, 885
- Gong Y., et al., 2019, *ApJ*, **883**, 203
- Hamilton A. J. S., 1992, *ApJ*, **385**, L5
- Hawkins E., et al., 2003, *MNRAS*, **346**, 78
- He S., Li Y., Feng Y., Ho S., Ravanbakhsh S., Chen W., Póczos B., 2019, *Proceedings of the National Academy of Science*, **116**, 13825
- Hockney R. W., Eastwood J. W., 1981, *Computer Simulation Using Particles*
- Isola P., Zhu J.-Y., Zhou T., Efros A. A., 2016, *arXiv e-prints*, p. [arXiv:1611.07004](#)
- Ivezić Ž., et al., 2019, *ApJ*, **873**, 111
- Jackson J. C., 1972, *MNRAS*, **156**, 1P
- Jing Y. P., Mo H. J., Börner G., 1998, *ApJ*, **494**, 1
- Kaiser N., 1987, *MNRAS*, **227**, 1
- Koda J., Blake C., Beutler F., Kazin E., Marin F., 2016, *MNRAS*, **459**, 2118
- Kodi Ramanah D., Charnock T., Lavaux G., 2019, *Phys. Rev. D*, **100**, 043515
- Laureijs R., et al., 2011, *arXiv e-prints*, p. [arXiv:1110.3193](#)
- Leauthaud A., et al., 2012, *ApJ*, **744**, 159
- Li Z., Jing Y. P., Zhang P., Cheng D., 2016, *ApJ*, **833**, 287
- Linder E. V., Cahn R. N., 2007, *Astroparticle Physics*, **28**, 481
- Lucie-Smith L., Peiris H. V., Pontzen A., Lochner M., 2018, *MNRAS*, **479**, 3405
- Lucie-Smith L., Peiris H. V., Pontzen A., 2019, *MNRAS*, **490**, 331
- Mandelbaum R., Seljak U., Cool R. J., Blanton M., Hirata C. M., Brinkmann J., 2006, *MNRAS*, **372**, 758
- Mao T.-X., Wang J., Li B., Cai Y.-C., Falck B., Neyrinck M., Szalay A., 2021, *MNRAS*, **501**, 1499
- Mathis H., Lemson G., Springel V., Kauffmann G., White S. D. M., Eldar A., Dekel A., 2002, *MNRAS*, **333**, 739
- Mo H. J., van den Bosch F. C., White S., 2010, *Galaxy Formation and Evolution* (Cambridge: Cambridge University Press)
- Modi C., Feng Y., Seljak U., 2018, *J. Cosmology Astropart. Phys.*, **2018**, 028
- More S., van den Bosch F. C., Cacciato M., Mo H. J., Yang X., Li R., 2009, *MNRAS*, **392**, 801
- Neistein E., Weinmann S. M., Li C., Boylan-Kolchin M., 2011, *MNRAS*, **414**, 1405
- Pan S., Liu M., Forero-Romero J., Sabiu C. G., Li Z., Miao H., Li X.-D., 2020, *Science China Physics, Mechanics, and Astronomy*, **63**, 110412
- Peacock J. A., Smith R. E., 2000, *MNRAS*, **318**, 1144
- Peacock J. A., et al., 2001, *Nature*, **410**, 169
- Pfeffer D. N., Breyse P. C., Stein G., 2019, *arXiv e-prints*, p. [arXiv:1905.10376](#)
- Planck Collaboration et al., 2020, *A&A*, **641**, A6
- Ravanbakhsh S., Oliva J., Fromenteau S., Price L. C., Ho S., Schneider J., Póczos B., 2017, *arXiv e-prints*, p. [arXiv:1711.02033](#)
- Rodríguez A. C., Kacprzak T., Lucchi A., Amara A., Sgier R., Fluri J., Hofmann T., Réfrégier A., 2018, *Computational Astrophysics and Cosmology*, **5**, 4
- Ronneberger O., Fischer P., Brox T., 2015, *arXiv e-prints*, p. [arXiv:1505.04597](#)
- Sargent W. L. W., Turner E. L., 1977, *ApJ*, **212**, L3
- Schmoldt I. M., et al., 1999, *AJ*, **118**, 1146
- Shi F., et al., 2016, *ApJ*, **833**, 241
- Shi F., et al., 2018, *ApJ*, **861**, 137
- Song Y.-S., Zheng Y., Taruya A., 2021, *Phys. Rev. D*, **104**, 043528
- Springel V., 2005, *MNRAS*, **364**, 1105
- Tassev S., Zaldarriaga M., Eisenstein D. J., 2013, *J. Cosmology Astropart. Phys.*, **2013**, 036
- Tinker J. L., Weinberg D. H., Zheng Z., Zehavi I., 2005, *ApJ*, **631**, 41
- Tröster T., Ferguson C., Harnois-Déraps J., McCarthy I. G., 2019, *MNRAS*, **487**, L24
- Tully R. B., Fisher J. R., 1978, in Longair M. S., Einasto J., eds, Vol. 79, *Large Scale Structures in the Universe*. p. 31
- Tweed D., Yang X., Wang H., Cui W., Zhang Y., Li S., Jing Y. P., Mo H. J., 2017, *ApJ*, **841**, 55
- Wang H., Mo H. J., Jing Y. P., Guo Y., van den Bosch F. C., Yang X., 2009, *MNRAS*, **394**, 398
- Wang H., Mo H. J., Yang X., van den Bosch F. C., 2012, *MNRAS*, **420**, 1809
- Wang H., Mo H. J., Yang X., van den Bosch F. C., 2013, *ApJ*, **772**, 63
- Wang H., Mo H. J., Yang X., Jing Y. P., Lin W. P., 2014, *ApJ*, **794**, 94
- Wang H., et al., 2016, *ApJ*, **831**, 164
- Wu Z., et al., 2021, *ApJ*, **913**, 2
- Wu Z., et al., 2023, *arXiv e-prints*, p. [arXiv:2301.04586](#)
- Yang X., Mo H. J., van den Bosch F. C., 2003, *MNRAS*, **339**, 1057
- Yang X., Mo H. J., van den Bosch F. C., Jing Y. P., 2005, *MNRAS*, **356**, 1293
- Yang X., Mo H. J., van den Bosch F. C., Pasquali A., Li C., Barden M., 2007, *ApJ*, **671**, 153
- Yang X., Mo H. J., van den Bosch F. C., 2008, *ApJ*, **676**, 248
- Yang X., Mo H. J., van den Bosch F. C., Zhang Y., Han J., 2012, *ApJ*, **752**, 41
- Yang X., et al., 2021, *ApJ*, **909**, 143
- York D. G., et al., 2000, *AJ*, **120**, 1579
- Zaroubi S., Hoffman Y., Fisher K. B., Lahav O., 1995, *ApJ*, **449**, 446
- Zhan H., 2011, *Scientia Sinica Physica, Mechanica & Astronomica*, **41**, 1441
- Zhang X., Wang Y., Zhang W., Sun Y., He S., Contardo G., Villaescusa-Navarro F., Ho S., 2019, *arXiv e-prints*, p. [arXiv:1902.05965](#)
- Zheng Z., et al., 2005, *ApJ*, **633**, 791
- van den Bosch F. C., Yang X., Mo H. J., 2003, *MNRAS*, **340**, 771
- van den Bosch F. C., et al., 2007, *MNRAS*, **376**, 841

This paper has been typeset from a $\text{\TeX}/\text{\LaTeX}$ file prepared by the author, and compiled using MNRAS \LaTeX style file v3.0